School of Medicine

Department of Health Sciences

Master's degree in medical biotechnologies

Laboratory of Immunomics

(Center for Translational Research on Autoimmune and Allergic Diseases-CAAD)

Characterization of rheumatoid arthritis fibroblast-like synoviocytes in a three-dimensional synovium-on-a-chip using immunofluorescence imaging

Relator: Prof. Annalisa Chiocchetti

Supervisor: Prof. Giuseppe Cappellano.

Firmato digitalmente da Annalisa Angela Chiocchetti
Data: 30.09.2026 17:02:40 CEST
Ente certificatore: UNIVERSITA' DEGLI STUDI DEL PIEMONTE ORIENTALE/01943490027

Candidate: Zeeshan Ahmad

Matricula Number: 20063822

Academic year 2025-2026

Table of Contents

ABSTRACT *1*

1. INTRODUCTION *2*

1.1. RA **2**

1.2. Synovium in RA **4**

1.3. RA Models **5**

1.3.1. *In vitro* models of RA 5

1.3.2. 2D culture and co-culture approaches 6

1.3.3. Organ-on-a-chip (OoC) 7

2. OBJECTIVES *9*

3. Methods and Materials *10*

3.1. Cell-hydrogel scaffold preparation and encapsulation on a chip **10**

3.2. Characterization and functionality of RA-FLSs on chip **10**

3.3. Characterization and functionality of RA-FLSs on chip under inflammatory stimuli **10**

3.3.1. Calcein-AM/PI staining for cell viability 10

3.3.2. Lubricin staining for cell functionality 10

3.3.3. CD55/CD90 staining for cell phenotypes 11

3.4. Image processing and analysis **11**

3.4.1. Viability analysis 12

3.4.2. Quantification of lubricin fluorescence 13

3.4.3. CD90/CD55 analysis 14

3.5. Statistical Analysis **15**

4. Results *16*

4.1. Development and application of the quantitative image-analysis workflow **17**

4.2. Microfluidic culture supports RA-FLS viability and functionality **19**

4.3. Spatial organization and functional stratification of RA-FLS within the SoC 21

4.4. Spatial organization and functional stratification of RA-FLS under inflammatory conditions 23

4.5. Dynamic response of the SoC to inflammatory stimulation 25

5. Discussion 28

ACKNOWLEDGMENT 33

REFERENCE 35

ABSTRACT

Rheumatoid arthritis (RA) is a chronic autoimmune disease characterized by persistent synovial inflammation, progressive cartilage destruction, and bone erosion. RA fibroblast-like synoviocytes (RA-FLSs) play a central role in disease progression by promoting inflammation, extracellular matrix remodeling, and joint damage. Although conventional in vitro models have improved our understanding of RA pathophysiology, they do not accurately reproduce the dynamic, three-dimensional (3D) synovial microenvironment. Therefore, developing physiologically relevant synovium-on-a-chip (SoC) platforms has emerged as a promising strategy for studying RA and evaluating therapeutic responses. This study aimed to develop and characterize a hydrogel-based SoC model for RA by evaluating RA-FLSs viability, spatial organization, phenotypic heterogeneity (CD55 and CD90), lubricin functionality, and inflammatory responses. RA-FLSs isolated from RA patients were encapsulated within a 3D hydrogel and cultured in a microfluidic SoC platform under physiological and inflammatory conditions. Cell viability was assessed using a Live/Dead fluorescence assay, while fibroblast phenotype and function were evaluated by immunofluorescence staining of CD55, CD90, and lubricin. Fluorescence images were processed using Fiji/ImageJ, and quantitative image analysis was performed using custom Python and Fiji/ImageJ workflows. The SoC platform successfully supported the formation of a viable 3D RA-FLSs microtissue, maintaining high cell viability and characteristic fibroblast morphology throughout the hydrogel. Analysis of CD55 and CD90 expression demonstrated the preservation of fibroblast phenotypic characteristics within the engineered construct, with CD90 displaying a significant spatial distribution across the microtissue, while lubricin expression confirmed the maintenance of fibroblast functional activity under physiological conditions. Inflammatory stimulation significantly reduced lubricin expression without markedly affecting overall cell viability, indicating functional impairment of RA-FLSs. In conclusion, the developed SoC model provides a physiologically relevant 3D platform that preserves RA-FLSs viability, phenotypic characteristics, and functional activity while reproducing key pathological features of RA under inflammatory stimulation. These findings support the use of the model as an in vitro platform for investigating RA-FLSs disease-associated functional changes.

1. INTRODUCTION

1.1. RA

RA is a chronic autoimmune condition characterized by systemic inflammation that affects the joints and multiple organ systems (Radu and Bungau, 2021). RA occurs in about 0.5% of the population, leading to severe joint damage and compromised physical function (Aletaha and Smolen, 2018). RA is characterized by the production of autoantibodies, primarily rheumatoid factor (RF) and anti-citrullinated peptide antibodies (ACPA), that target widely distributed self-antigens across the joints. It is also a chronic inflammatory condition led by numerous cytokines that function both correlatively and simultaneously, a feature referred to as overlap within the cytokine network (Boissier, 2011).

The prevalence of RA varies across regions, often being higher in developed countries due to environmental risks, genetic factors, population-based differences, and incomplete reporting in other regions (Finckh et al., 2022). Genetic factors play a role in the development of RA from early life, with the strongest links found in females and individuals with a family history of the disease. Environmental factors and various health conditions are linked to RA, with recent evidence highlighting gene–environment interactions. Comorbidities, like obesity and diabetes mellitus, are known to increase the risk of developing RA, although their predictive value is low (van Boheemen and van Schaardenburg, 2019). Furthermore, various mechanisms have been proposed to explain tissue damage in RA, immune complexes are likely the first fundamental cause (Weissmann, 2004).

Both musculoskeletal and general symptoms have been linked to RA, including joint pain and swelling, along with warmth, redness, and burning sensations around the joints. Others include early morning stiffness, muscle weakness, reduced motor function, fatigue, sleep disturbances, and depressive symptoms (van Boheemen and van Schaardenburg, 2019).

Over the past two decades, major advances have been made in understanding RA pathophysiology, enhancing outcome measures, and developing effective treatments, with a growing focus on early diagnosis and management (Aletaha and Smolen, 2018). While recent advances in RA therapy may lead to enhanced life-saving in the future, factors such as sustained low-grade inflammation,

comorbidities, and immunogenetic influences may still contribute to increased mortality and limit this progress (Myasoedova et al., 2010).

Managing RA calls for a clear-eyed, critical approach. Disease activity needs to be checked again and again, so treatment can be adjusted as needed, staying aligned with a “treat to target” strategy (Szmyrka and Szechinski, 2001). Escalating therapy needs to be matched closely to who the patient is and what risks come with the treatment plan. For RA patients, starting drug therapy promptly, especially in the first year after diagnosis, tends to pay off, much like it does in other long-running conditions. When extra-articular features show up, the approach usually must cover both the here-and-now and the long haul, most often with disease-modifying anti-rheumatic drugs (DMARDs), corticosteroids, and nonsteroidal anti-inflammatory drugs (NSAIDs). NSAIDs can ease pain and stiffness and help patients move and function better, but they don’t stop joint damage itself. Glucocorticoids, by acting on the disease’s underlying drivers, can calm symptoms fast and have disease-modifying effects, yet the downside is that extended use carries major adverse effects. DMARDs, on the other hand, are chosen to bring inflammation down and to slow structural deterioration over time. Broadly, DMARDs fall into two groups, synthetic and biological, and synthetic DMARDs are commonly split again into conventional synthetic and targeted synthetic types (Smolen et al., 2014).

Methotrexate (MTX) is the synthetic DMARDs most often prescribed for RA, largely because it works well at shifting the Th1/Th2 balance toward Th2 expansion (Monserrat Sanz et al., 2020). By blocking dihydrofolate reductase, it dampens inflammation and slows disease activity, since purine and pyrimidine production drops and IL-6 levels come down as well. For RA, the European Alliance of Associations for Rheumatology (EULAR) advises beginning therapy with MTX and pairing it with low-dose glucocorticoids, a recommendation backed by solid evidence. When different treatment strategies have been put side by side in studies, results have largely lined up, with no approach showing a clear, meaningful edge over the others (Nam et al., 2014). Glucocorticoids can be given by mouth at low to moderate doses, or as a one-time intravenous or intramuscular shot, particularly when paired with MTX to add extra structural protection (Antoni et al., 2005).

1.2. Synovium in RA

The synovium is a soft connective tissue that lines the chambers of synovial (diarthrodial) joints, as well as tendon sheaths and bursae. It consists of two main elements: a surface layer known as the intima and a deeper layer called the subintima. The intima is made up of specialised FLS along with synovial macrophages, while the subintima contains blood and lymphatic vessels, along with resident FLS and infiltrating immune cells integrated within a collagen-rich extracellular matrix (Smith and Wechalekar, 2015). In healthy tissue, FLS play a key role in maintaining joint homeostasis by providing the joint cavity and adjacent cartilage with fundamental plasma-derived nutrients and lubricating substances, including hyaluronic acid. They also assist in ongoing extracellular matrix turnover by synthesizing structural components like collagen and hyaluronan, while concurrently secreting enzymes that regulate matrix degradation (Müller-Ladner et al., 2007).

In RA, the synovium is the major site of inflammation, and without treatment, this can cause permanent deterioration of surrounding cartilage and bone. It is now well recognized that RA-specific autoantibodies, such as RF and ACPA, occur before clinical symptoms develop (Boissier, 2011). Once synovitis in RA is identified, various reinforcement processes help sustain inflammation and encourage disease persistence (Hitchon and El-Gabalawy, 2011). Proinflammatory cytokines play a role in the early stages of inflammation within the rheumatoid synovium. Although the accurate triggers of rheumatoid synovitis are not fully understood, both antigen-specific and non-antigen-specific pathways are thought to participate. Activated T lymphocytes, particularly those expressing human leukocyte antigen DR4. (HLA–DR4) with the shared major histocompatibility complex (MHC) epitope, are thought to be important in initiating the pathological process (Arend, 2001).

RA-FLSs are the major cell types in the outer layer of the thickened synovial tissue that sweeps and destroys nearby cartilage and bone. They play an active role by enhancing inflammation and joint breakdown through the release of pro-inflammatory cytokines and enzymes that degradate the extracellular matrix (Müller-Ladner et al., 2007). Evidence suggests that chondrocytes are not merely reactive targets in cartilage injury but also actively contribute to matrix degradation. They respond to proinflammatory cytokines sourced from the synovium and can also produce such cytokines themselves. Through autocrine and paracrine signaling, these mediators promote tissue

breakdown while inhibiting repair mechanisms. This imbalance between catabolic and anabolic processes likely plays a major role in the accelerated loss of cartilage matrix seen in RA, with the main cytokine-mediated interaction involved in RA pathogenesis summarized in **(Figure 1)** (Otero and Goldring, 2007).

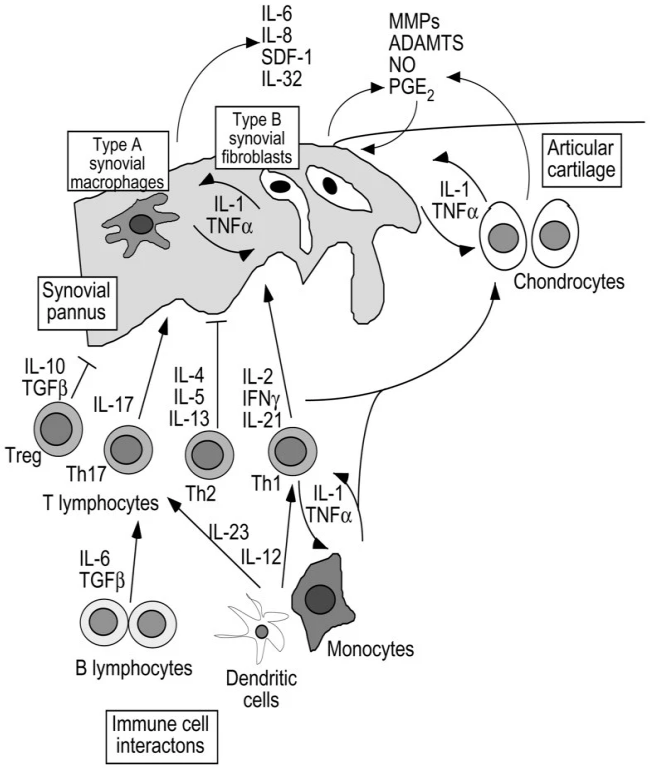

Fig. 1. Cytokine network involved in the pathogenesis of RA. Pro-inflammatory cytokines, including TNF-α, IL-1, IL-6, IL-17, and IFN-γ, produced by immune cells and RA-FLSs promote synovial inflammation, cartilage degradation, and bone destruction. Anti-inflammatory mediators such as IL-4, IL-10, IL-13, TGF-β, and IL-1 receptor antagonist (IL-1Ra) counteract these inflammatory pathways and contribute to the regulation of immune responses and tissue homeostasis (Otero and Goldring, 2007).

1.3. RA Models

1.3.1. *In vitro* models of RA

There are numerous preclinical models of RA available; many have limited predictive precision because they depend on distantly related animals. Over the past decade, advances in tissue engineering have considerably enhanced in vitro techniques for studying RA. As a result, the disease's pathogenesis has been shaped using a wide range of both in vitro and in vivo systems.

Cell-based in vitro approaches vary from tissue explants and simple 2D (co)culture models to more advanced 3D engineered systems composed of multiple cell types. These cells may be obtained from established cell lines, primary sources, or patient-derived materials such as mesenchymal stromal cells (MSCs) and induced pluripotent stem cells (iPSCs). Such models are used to examine processes including cell migration, activation, antigen presentation, cell–cell interactions, and alterations in both cellular behavior and extracellular matrix structure (Damerau and Gaber, 2020).

Furthermore, organoids cultured on microfluidic chips, along with computational (in silico) models, represent promising tools for enhancing the understanding of RA pathophysiology and identifying new treatment targets. Future preclinical in vitro screening platforms are planned to rely on microphysiological human joint-on-a-chip systems that integrate primary cells from RA patients and various organs. These models aim to reproduce the systemic nature of the disease, enhance translation to human implementation, and reduce dependence on animal testing **(Figure 2)** (Damerau and Gaber, 2020).

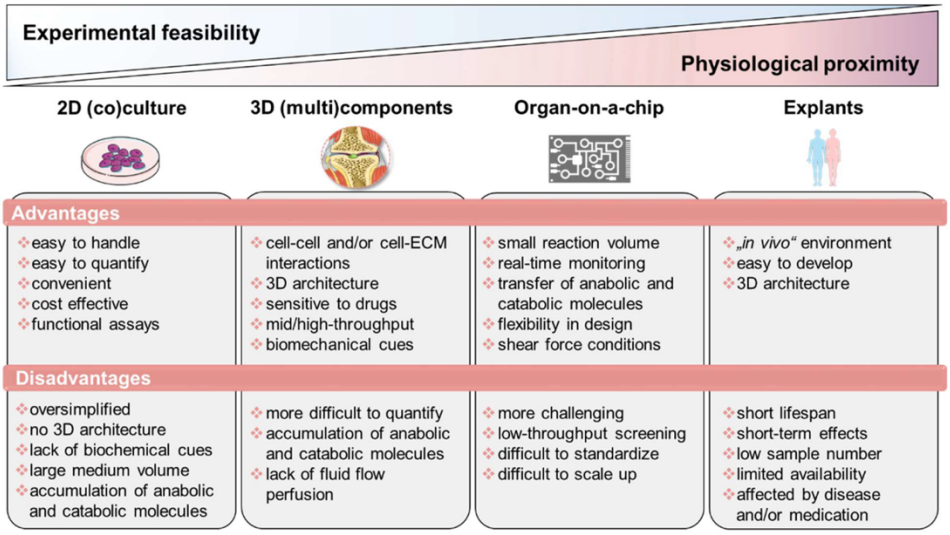

Fig.2. Overview of state-of-the-art in vitro models classified according to experimental feasibility and physiological proximity. Figure contains graphics from Servier Medical Art, licensed under a Creative Commons Attribution 3.0 Generic License. **http://smart.servier.com/**.(Damerau and Gaber, 2020).

1.3.2. 2D culture and co-culture approaches

Precisely replicating the physiological and pathological complications of biological systems often requires the use of tissue explants or advanced 3D tissue models that maintain structural

organization. 2D monolayer cultures are commonly used for rapid in vitro cell enlargement, although they may cause changes in cell morphology, genetics, diversity, cell cycle behavior, and differentiation potential (Damerau and Gaber, 2020).

By extending 2D monolayer cultures into co-culture systems, exchange between cells within the same environment can be investigated either indirectly, using physical separation methods such as medium transfer or transwell chambers, or directly through mixed cultures that allow cell-to-cell contact. Using both methods, human RA-FLSs suppressed the tumor necrosis factor-alpha (TNF-α)–induced interferon-gamma (IFN-γ) response in macrophages under both direct and indirect conditions. Due to this, direct cell contact is not necessary, and soluble factors released by fibroblasts are responsible for inhibiting the macrophage IFN-γ signature (Donlin et al., n.d.).

3D models provide important advantages over traditional 2D systems, as they better assist cell–cell and cell–matrix interactions, as well as processes such as cell proliferation, differentiation, and migration, while preserving cellular behavior within a more physiologically relevant environment. To precisely replicate joint structure, an essential condition for modeling RA pathogenesis, various cellular components, including the synovial membrane and the cartilage, and bone-forming (chondrogenic and osteogenic) elements, need to be integrated into 3D in vitro systems (Damerau and Gaber, 2020).

1.3.3. Organ-on-a-chip (OoC)

In recent years, infusion-based culture systems have gained increasing significance due to their ability to support the development of functional tissues. These systems provide a continuous delivery of nutrients and enable precise, real-time control of environmental parameters such as pH, temperature, and oxygen levels. Additionally, multi-chamber bioreactors enable the controlled co-culture of two or more cell or tissue types within a defined environment. (Lin et al., 2014).

In general, microfluidic systems offer high design flexibility, enabling the creation of controlled concentration gradients, accurate spatial arrangement of cells, and tailored co-culture and shear stress conditions (Mestres et al., 2019). Currently, only a small number of microfluidic culture methods can partially replicate joint physiology by modeling subchondral bone, articular cartilage, or the osteochondral region, as well as the synovial membrane, including its spatial and mechanical characteristics **(Figure 3)** (Rosser et al., 2019).

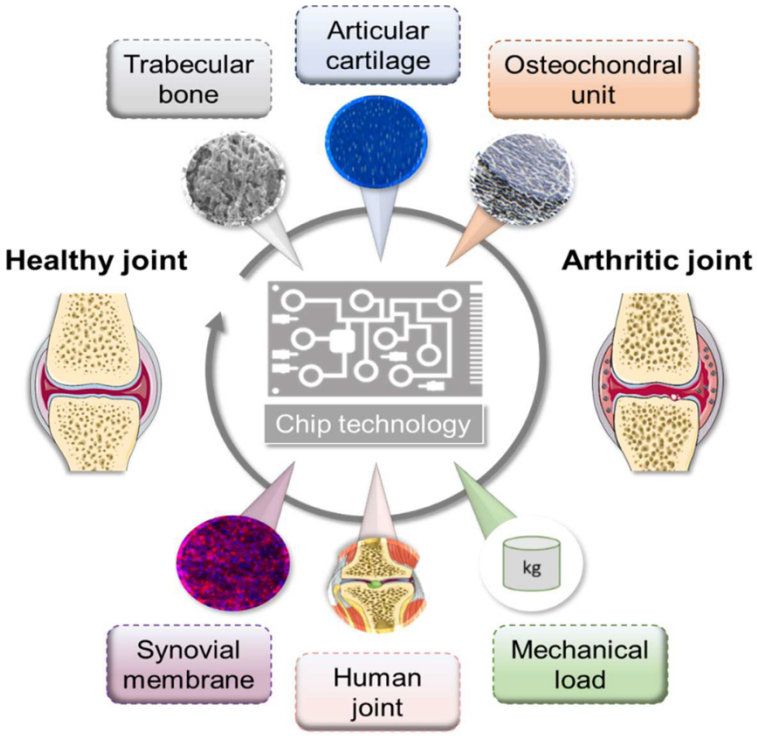

Fig.3 Overview of microfluidic approaches mimicking selected physiological interactions of the human joint tissues. The figure was modified from Servier Medical Art, licensed under a Creative Commons Attribution 3.0 Generic License. **http://smart.servier.com/**. (Celikkin et al., 2021).

An OoC is a microfluidic cell culture platform consisting of continuously infused and/or mechanically promoted microchambers or channels that assemble living cells arranged in three dimensions to replicate the structure and function of tissues and organs. In tissue engineering and regenerative medicine, biofabrication has become a key method for recreating the complex architecture and scale of human organs, providing benefits such as precise, automated production of physiologically relevant 3D tissues with high reproducibility (Celikkin et al., 2021). Among many techniques to analyze OoC, immunofluorescence is a technique in which fluorescently marked antibodies are used to evaluate the expression of target antigens (Odell and Cook, 2013), supplementing clinical evaluation and histopathological analysis for diagnosing autoimmune diseases. They facilitate timely identification, guide treatment determinations, and support ongoing evaluation of disease progression in affected patients (Mohan et al., 2008).

2. OBJECTIVES

This internship was carried out at the Immunomics laboratory (Head Prof. Annalisa Chiocchetti), and it is part of the FLAMIN-GO project (Grant Agreement No. 953121), funded by the European Union's Horizon 2020 programme. The aim of this thesis concerned the development, optimization, and application of an image-analysis pipeline for the quantification of immunofluorescence images obtained from RA-FLSs cultured within the SoC model. My contribution focused on image processing and quantitative analysis using Fiji/ImageJ and Python-based computational tools to extract quantitative measurements from fluorescence images.

The image analysis workflow was applied to investigate cell viability, FLS phenotypes, and cellular functions of RA-FLSs under experimental conditions applied in the SoC model. Specific quantitative analysis of live/dead cell distributions and the levels of expression of the fibroblast markers CD55 and CD90 and lubricin will be described in the thesis. The developed analytical approach was used to compare RA-FLSs when cultured under static and microfluidic conditions, to investigate their spatial organization across different regions of the SoC, and to quantify changes associated with inflammatory stimulation.

The final aim of this thesis was to provide a structured and reproducible image-analysis method capable of reporting qualitative data for the SoC model, extracted from fluorescence microscopy images and interpreted based on their biological significance.

3. Methods and Materials

3.1. Cell-hydrogel scaffold preparation and encapsulation on a chip

RA-FLSs suspended in media culture ($5x10^6$ cells/mL RA-FLS) were mixed gently with GelMA-LAP solution to reach a working solution of 5% and 0.3%, respectively. Then, the bioink was embedded in the synovial chamber of the SoC or in a plate (static condition) and exposed to UV irradiation for 1 minute to enable GelMA's photocrosslinking. Subsequently, the SoC was sealed tightly with a PDMS membrane and screws, and the inlet and outlet tubes were connected to perfuse the media. Complete DMEM/F12 medium was used to culture RA-FLSs on the chip.

3.2. Characterization and functionality of RA-FLSs on chip

SoCs were cultured under continuous perfusion (40 µl/hour) using a mechanical microfluidic pump in an incubator at 37°C, 5% CO2. After 3 days of encapsulation, cell viability, functionality, and phenotype were assessed using Calcein-AM/PI staining, lubricin staining, and CD55/CD90 staining, respectively.

3.3. Characterization and functionality of RA-FLSs on chip under inflammatory stimuli

To mimic the inflammatory microenvironment characteristic of RA conditions, the culture medium was supplemented with pro-inflammatory cytokines, namely TNF-α (20 ng/mL), IL-1β (10 ng/mL), and IL-6 (10 ng/mL). Cytokine stimulation was initiated 18 h after cell encapsulation on the chip and maintained for approximately 54 h to induce an inflammatory response. After 3 days of encapsulation, we evaluated the readouts described in 3.2. On-chip immunofluorescent staining.

3.3.1. Calcein-AM/PI staining for cell viability

Calcein-AM (3 µM) (BD Biosciences, USA) and PI (50 µg/mL) (Sigma-Aldrich, Germany) resuspended in PBS 1X were fluxed into the chip for 20 minutes at 37°C in the dark at 40 µl/hour. The chip was washed with PBS 1X before and after staining for 10 minutes at the same speed. Viable cells emitted green fluorescence at excitation/emission set at 488/530 nm, whereas nuclei of dead cells appeared red at 530/580 nm.

3.3.2. Lubricin staining for cell functionality

BD GolgiPlug™ Protein Transport Inhibitor (1:1000; BD Sciences) were fluxed into the chip for at least 4 hours to keep the lubricin inside the cells and then fixed with 4% paraformaldehyde

(PFA; Sigma-Aldrich, Germany) in PBS 1X for 20 minutes. The cells were then permeabilized with 0,2% Triton (Sigma-Aldrich, USA) in PBS 1X for 15 minutes and blocked with 4% Bovine Serum Albumin (BSA; Merck) in PBS 1X for 30 minutes. Primary antibody (anti-Lubricin 1:500 - Thermofisher) diluted in 1% BSA was added and incubated for 2 hours. Subsequently, secondary antibody (Goat anti-Rabbit IgG (H+L) Cross-Adsorbed Secondary Antibody, Alexa Fluor™ 488 1:500 - Thermofisher) diluted in 1% BSA was added for 1 hour. Finally, HOECHST (1:250; Thermofisher) in PBS 1X was added for 15 min. Between and after each step, the chips were carefully washed with PBS 1X for at least 5 min. Every step was performed by gently adding the solutions to the fluidic system of the SoC. The lubricin^{+} emitted green fluorescence at excitation/emission set at 488/530 nm, whereas the cell nuclei emitted blue fluorescence at excitation/emission set at 355/450 nm.

3.3.3. CD55/CD90 staining for cell phenotypes

Cells encapsulated inside the SoC were fixed with 4% PFA in PBS 1X for 20 minutes. The hydrogels with cells were then blocked with 4% BSA in PBS 1X for 30 minutes. Then, antibodies anti-CD55 (Monoclonal antibody (Bu14; CD55) – FITC 1:100 – Thermo Fisher) and anti-CD90 (APC- Mouse anti-human CD90 1:100; Thermo Fisher), diluted in 1% BSA, were added and incubated for 1 hour and 30 minutes. Subsequently, HOECHST 1:250 in 1% PBS was added for 15 min. Between and after each step, the chips were carefully washed with PBS 1X for at least 5 min. Every step was performed by gently adding the solutions to the fluidic system of the SoC. The CD55+ emitted green fluorescence at excitation/emission set at 488/530 nm, whereas the CD90+ emitted far-red fluorescence at excitation/emission set at 650/660 nm, and the cell nuclei emitted blue fluorescence at excitation/emission set at 355/450 nm.

Images after all the staining were acquired using a Leica THUNDER Imager 3D Live Cell in brightfield and fluorescence channels at an objective magnification of 20X.

3.4. Image processing and analysis

Images after the staining were acquired using a Leica THUNDER Imager 3D Live Cell in brightfield and fluorescence channels at an objective magnification of 20X. High-resolution Z-stacks were acquired at 20X magnification to encompass the full depth of the 3D microenvironment. Raw imaging data (TIFF format) underwent background subtraction and were

collapsed into maximum intensity projections (MIP) using ImageJ (NIH) to facilitate downstream quantitative analysis.

For analyzing spatial organization, phenotype, and functional output of FLS within the 3D microenvironment, Z-stack imaging data (TIFF format) underwent background subtraction and enabled the arbitrary subdivision of the microtissue into three distinct regions, defined as top (adjacent to the PDMS membrane), middle, and bottom layers using Fiji/ImageJ software (version 1.54p; Wayne Rasband and contributors, NIH, Bethesda, MD, USA) to facilitate downstream quantitative analysis.

3.4.1. Viability analysis

Images were produced from fluorescence Z-stacks in Fiji/ImageJ and then measured quantitatively with a custom image-analysis workflow implemented in Python 3. Image acquisition varied by experiment; the analysis was based on two fluorescence channels: the green channel (Ch01) corresponded to Calcein-AM, marking viable cells, while the red channel (Ch02) corresponded to Propidium Iodide (PI), marking non-viable cells.

Images from the two channels of fluorescence were paired according to their filenames and analyzed separately. Prior to segmentation, fluorescence images were intensity-normalized between the 1st and 99.8th percentiles to improve consistency in objects across images. To quantify viability, a deep learning segmentation workflow was run in Python 3. Live and dead cells were detected automatically using the StarDist2D deep learning framework with the pretrained 2D versatile fluo model. The same segmentation parameters were applied to both channels, with a probability threshold (prob_thresh) of 0.7 and a non-maximum suppression threshold (nms_thresh) of 0.0.

After image analysis by StarDist, an instance segmentation mask was created for every fluorescence image, and the number of identified particles was automatically extracted. The number of objects identified in the Calcein-AM, green channel (Ch01) image was attributed to the number of viable cells, and the number of objects identified in the PI, red channel (Ch02) was attributed to dead cells.

For each image, the numbers of viable and dead cells obtained from the segmented Calcein-AM and PI channels were used to calculate cell viability according to the formula:

$$Cell\ Viability\ (\%) = \frac{Number\ of\ viable\ cells}{Total\ number\ of\ cells} \times 100$$

where the total number of cells corresponds to the sum of viable and dead cells.

For each image, the automated pipeline produced quantitative cell counts, and those values were then carried forward into GraphPad Prism for statistical processing. The same workflow was kept in place for every condition tested, covering both static and microfluidic culture formats in physiological as well as inflammatory environments.

3.4.2. Quantification of lubricin fluorescence

Lubricin expression was measured from fluorescence microscopy images by measuring the intensity of the lubricin-specific signal in the green channel (Ch01). Quantification was performed using pixel-based analysis in Fiji/ImageJ, based on the principle that fluorescence intensity is proportional to the amount of labeled protein.

For each image, the signal was segmented using the Otsu automatic thresholding technique, resulting in the creation of a binary mask separating the positive cells from the background, which was then used to quantify cell-specific fluorescence. Then, fluorescence measurements were obtained using the "Set Measurements" function in Fiji/ImageJ. Among these parameters, Integrated Density (IntDen) was used as the quantitative measure of lubricin fluorescence. Integrated Density represents the sum of all pixel intensity values within an analyzed region and therefore provides a measure of the total fluorescence signal associated with lubricin expression.

Integrated density is calculated by the following equation:

$$Integrated\ Density\ (IntDen) = Area\ \times\ Mean\ Gray\ Value$$

For each image, the fluorescence signal corresponding to lubricin expression was quantified by adding the IntDen values across all detected cellular regions:

$$Total\ Lubricin\ Intensity = \sum IntDen$$

Since variation in the number of cells found in each image can affect the overall level of fluorescence, values of lubricin fluorescence were then normalized to account for variations in cell counts between each image. This normalization represented lubricin expression relative to the amount of cellular material in each image analyzed, thus making the values comparable between experimental conditions.

Cell quantification was determined using the nuclear fluorescence channel (ch02) to account for differences in cell density among images, which allowed accurate identification of individual cells based on fluorescence signal.

Nuclear Images were processed in Fiji/ImageJ by converting the corresponding channel to 8-bit grayscale and applying threshold-based segmentation to differentiate nuclei from background noise. Following threshold-based segmentation, the resulting binary images were used for automated cell detection, which was carried out using the "Analyze Particles" function in Fiji/ImageJ, which identifies separate objects based on predefined size and intensity criteria. This method enabled consistent and replicable detection of nuclei across all samples. The resulting cell count was used to normalize the total lubricin fluorescence intensity.

Because total lubricin fluorescence intensity is influenced by the number of cells present in the image, normalization was applied to consider variations in cell density between samples. Specifically, total lubricin fluorescence intensity (calculated as the sum of Integrated Density values from the lubricin channel, ch01) was normalized to the total cell count obtained from the nuclear channel.

To normalize fluorescence intensity to cell number, normalized lubricin expression was calculated as:

$$Normalized\ Lubricin\ Expression = \frac{Total\ Lubricin\ Intensity\ (ch01)}{Total\ Cell\ Count\ (ch02)}$$

3.4.3. CD90/CD55 analysis

CD55 and CD90 expression was quantitatively assessed from immunofluorescence images using Fiji/ImageJ. Specifically, for each of the phenotypic markers, its fluorescence channel was measured, and the corresponding cell numbers were acquired using the cell nuclear channel (Hoechst-stained) as described in section 3.5.2.

For each marker, raw fluorescence images were converted into 8-bit grayscale and segmented from the background by Otsu's automatic thresholding method. Using the thresholded fluorescence-

positive areas, we quantified the intensity associated with the marker. The IntDen was acquired as the intensity value, the total intensity summed within the identified positive regions.

In order to take cell density differences into account in each picture, the sum of the fluorescence intensity measured for each marker was divided by the sum of nuclei detected in each field. For CD55 and CD90, expression per cell can be quantified according to the following equation :

$$Normalized\ marker\ expression = \frac{total\ marker\ fluorescence\ intensity}{total\ cell\ count}$$

A similar method for imaging and quantification was applied reproducibly to images of both CD55 and CD90 for the different experimental conditions and separately to the top, middle, and bottom regions of the image when analysis focused upon spatial aspects of the SoC.

3.5. Statistical Analysis

Statistical analyses were performed using GraphPad Prism version 9.0.0 (121) (GraphPad Software, San Diego, CA, USA). Quantitative data obtained from image analysis were organized according to the experimental comparison and are presented as individual biological data points together with the mean ± standard error of the mean (SEM).

Before statistical comparisons, data distribution was assessed using the Shapiro–Wilk normality test with a significance level of $\alpha = 0.05$. Statistical tests were selected according to data distribution and experimental design. The specific statistical test used for each experiment is indicated in the corresponding figure legend. A value of $P < 0.05$ was considered statistically significant. Statistical significance is indicated in the figures using asterisks: *$P < 0.05$, **$P < 0.01$, and ***$P < 0.001$, while non-significant differences are indicated as ns.

4. Results

The experimental results were arranged to test how the SoC model behaves across different culture conditions. To begin with, RA-FLSs grown in standard static culture were compared to cells maintained in the microfluidic SoC device, with the focus placed on potential shifts in viability and in lubricin expression. After that initial comparison, the SoC model was examined more broadly, both in structure and in functional characterization by evaluating cell viability, morphology, spatial distribution, the presence of fibroblast phenotype markers (CD55 and CD90), and lubricin expression throughout the engineered microtissue. Finally, inflammatory stimulation was introduced to see how the SoC model reacts, tracking any resulting changes in viability, fibroblast phenotype, and lubricin expression **(Figure 4).**

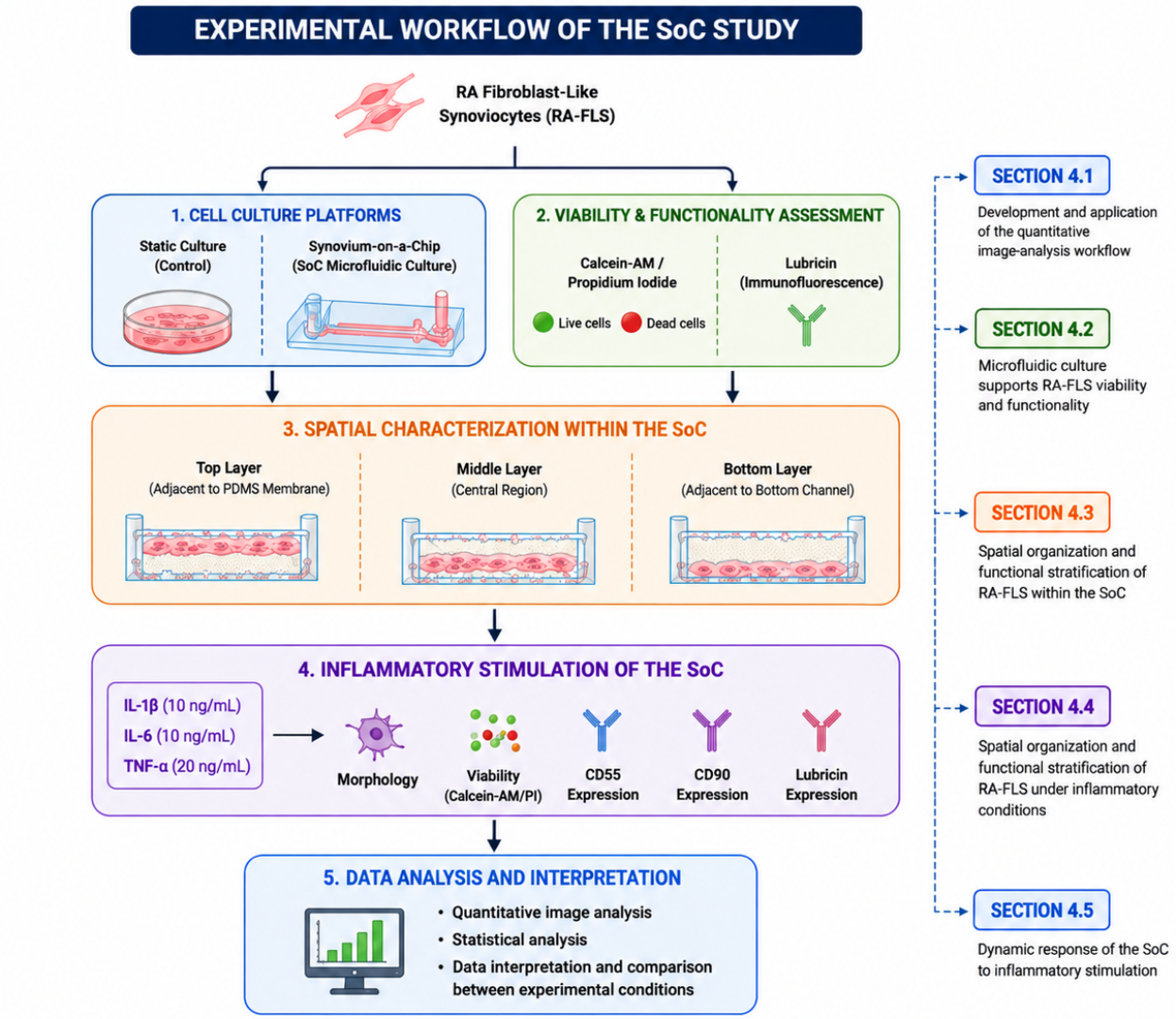

Fig.4. Experimental workflow of the SoC study. RA-FLSs were cultured under conventional static conditions and within a microfluidic SoC platform. Cell viability and functionality were assessed, followed by spatial characterization of the SoC across the top, middle, and bottom layers. Subsequently, the SoC was exposed to inflammatory cytokines (IL-1β, IL-6, and TNF-α) to evaluate morphological, viability, phenotypic (CD55 and CD90), and functional (lubricin) responses. Finally, quantitative image analysis and statistical evaluation were performed to interpret the results and compare experimental conditions.

4.1. Development and application of the quantitative image-analysis workflow

Quantitative analysis of the SoC fluorescence imaging data was performed using an image-analysis workflow that was specifically custom-designed and optimized for the present study. The main purpose was to convert the images of RA-FLSs in the fluorescence images into quantitative and repeatable measures of cell viability, cell phenotype, and cell function. Emphasis was placed on selecting image processing and quantification methods that would be suitable for use throughout SoC regions and with varying experimental conditions.

Raw fluorescence images were organized based on experimental condition, biological donor, staining, and imaging region. The Z-stack acquisitions were analyzed to generate maximum intensity projection images, and each fluorescence channel was analyzed individually based on the parameter of interest. To quantify cell viability, the Calcein-AM signal was utilized to differentiate viable cells, and the propidium iodide signal to differentiate dead cells, and an automated image-analysis pipeline was used to obtain the total number of cells counted. In parallel, to analyze the immunofluorescence response, CD55, CD90, and lubricating fluorescence signal intensities were measured using Fiji/ImageJ, and the total fluorescent intensity measurements were subsequently normalized to the corresponding cell number where required.

The analysis was performed in a similar way to investigate spatial heterogeneity across the 3D microtissue, on images for the top, middle, and bottom areas of SoC. This process standardizes the quantitative readings in terms of fluorescence obtained from the regions and from the experiments and minimizes variability that can arise from manual image review. The data obtained in numerical form were organized and transferred to GraphPad Prism for statistical analysis and visualization. The complete quantitative image-analysis workflow, from fluorescence image preprocessing and cell/marker detection to quantitative measurement, normalization, and generation of the final datasets for statistical analysis, is summarized in **(Figure 5).**

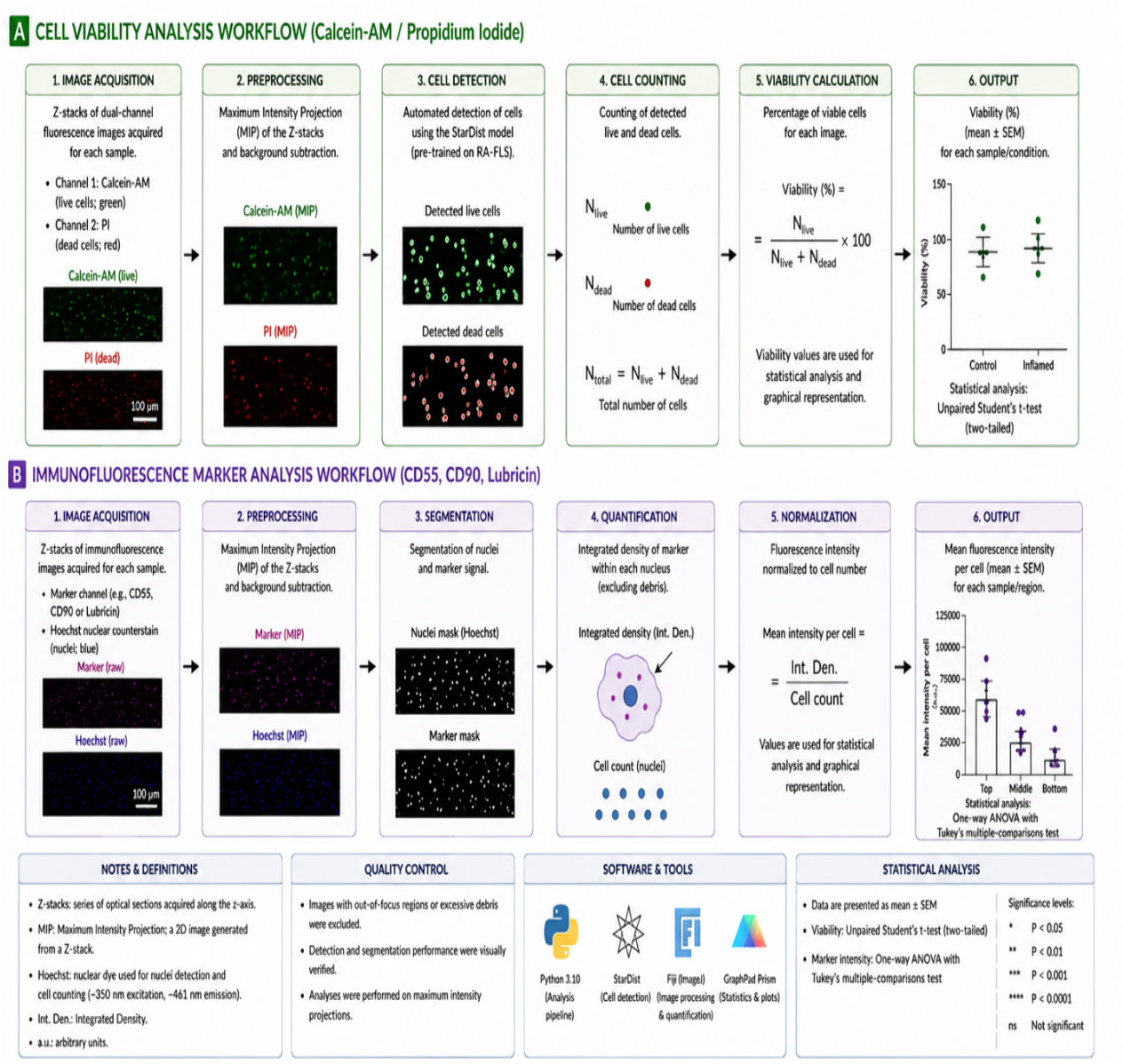

Fig. 5. Development and application of the quantitative image-analysis workflow. (A) Workflow for cell viability analysis using Calcein-AM (live) and Propidium Iodide (PI, dead). (B) workflow for immunofluorescence marker analysis (CD55, CD90, and lubricin) with Hoechst nuclear counterstain. The same analytical pipelines were applied to all experimental conditions and spatial regions (top, middle, bottom layers) under control and inflammatory conditions.

4.2. Microfluidic culture supports RA-FLSs viability and functionality

The impact of the microfluidic culture system on RA-FLSs viability and lubricin expression was assessed by fluorescence images acquired on RA-FLSs from both static and SoC cultures. Representative Calcein-AM/PI and lubricin staining are shown in **(Figure 5)** above and were

processed by the quantitative image analysis protocol. The analysis for viability was based on detection of live and dead cells in the Calcein-AM and PI channels, respectively, and was calculated as the percentage of live cells.

As shown in (**Figure 6A**), quantitative image analysis showed a high level of cell viability under both culture conditions, with comparable mean viability values. RA-FLSs cultured within the SoC showed a mean viability of 83.31 ± 2.17%, while cells maintained under static conditions showed a mean viability of 83.77 ± 6.83%. No statistically significant difference in mean cell viability was detected between the two culture conditions. However, the lower standard deviation observed in the SoC condition indicates that the viability measurements were less variable across the analyzed samples compared with static culture.

Next, cell function was quantified by measuring lubricin immunofluorescence intensity. Lubricin fluorescence intensity was quantified and normalized to the corresponding cell number to obtain fluorescence intensity per cell. RA-FLSs cultured on the SoC exhibited significantly more lubricin signal compared with cells maintained under static conditions. Lubricin fluorescence intensity of cells on the SoC increased from 29,069 ±7,358 intensity/cell in static culture to 51,922 ±6,122 intensity/cell in the SoC ($P < 0.05$). This difference is visualized in the representative fluorescence images below (**Figure 6B**), where lubricin staining is more pronounced and widely dispersed in the microfluidic condition.

Overall, these quantitative image-analysis data imply that the SoC maintained the viability of RA-FLS at a comparable level to standard static cultures, while supporting significantly greater lubricin expression. Representative fluorescence images and comparisons for both static and SoC cultures are presented in **(Figure 6).**

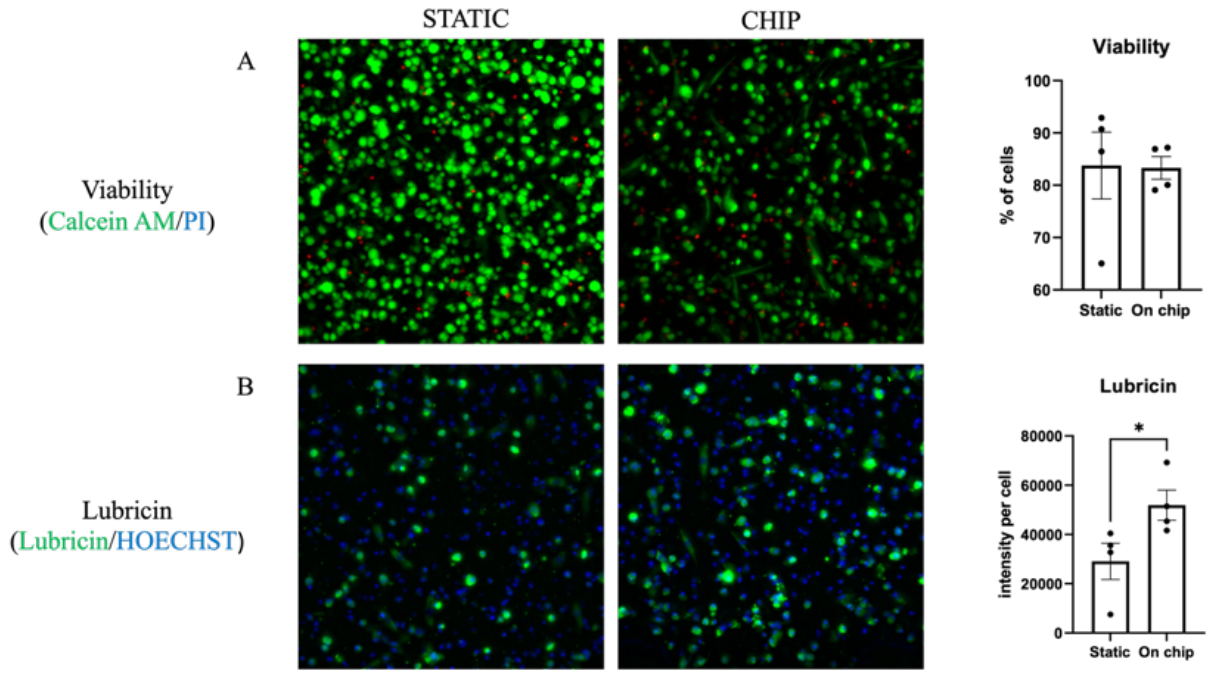

Fig. 6. Microfluidic culture enhances fibroblast functionality compared to static conditions: (A) representative MIP image showing viability of RA-FLSs (5 × 10^6 cells/mL in GelMA 5%) between 3D encapsulated DROP and CHIP configurations after 3 days (left panel). Quantitative comparison of viability, demonstrating high viability between the two conditions (right panel). (B) Representative MIP images showing lubricin assessment of RA-FLSs (5 × 10^6 cells/mL in GelMA 5%) between 3D encapsulated DROP and CHIP configurations after 3 days (left panel). Quantitative comparison of lubricin production, showing significantly higher levels in on-chip culture (right panel). Data are presented as mean ± SEM, n = 4 independent biological donors. Statistical significance was determined by an unpaired t-test or Mann-Whitney test, ∗P<0.05.

4.3. Spatial organization and functional stratification of RA-FLSs within the SoC

To assess the capability of the SoC to recapitulate relevant features of the microtissue, after three days of encapsulation within the SoC, RA-FLSs were assessed for viability, morphology, phenotype marker expression, and functional protein production (lubricin). To evaluate spatial variations within the platform, images of the SoC were acquired as Z-stacks in a Leica THUNDER fluorescent microscope, then divided into three different areas, obtained by dividing the microtissue into equal layers: top, adjacent to the polydimethylsiloxane (PDMS) membrane; middle; and bottom.

Live/dead staining with Calcein-AM/PI revealed high overall viability across all three layers, with no statistically significant differences detected among the spatial regions. Cell viability was 76.09 ± 5.37% in the top layer, 84.56 ± 4.35% in the middle layer, and 80.84 ± 3.79% in the bottom layer.

Although mean viability was slightly higher in the middle layer, repeated-measures one-way ANOVA showed that the differences were not statistically significant (**Figure 7D**).

Interestingly, cell distribution and morphology varied by depth across the microtissue: the top layer contained fewer cells overall, but were generally spindle-like and elongated, whereas the bottom one showed increased cell density, composed predominantly of rounded cells. Given these morphological differences, we analyzed the spatial distribution of CD55 and CD90. After 3 days, CD90 was more strongly expressed across all layers than CD55. CD90 expression was highest in the top layer and decreased toward the bottom layer of the SoC. The mean fluorescence intensity was 309,023 ± 40,324 intensity/cell in the top layer, 173,911 ± 78,670 intensity/cell in the middle layer, and 37,959 ± 22,441 intensity/cell in the bottom layer, respectively. Tukey's multiple comparison test demonstrated that CD90 expression was significantly higher in the top than in the bottom layer ($p < 0.05$), whereas no significant differences were detected between the top and middle layers or between the middle and bottom layers **(Figure 7F)**. CD55 expression was detected in all three layers of the SoC. The highest mean fluorescence intensity was observed in the middle layer, 41,453 ± 12,758 intensity/cell, compared with the top layer 25,274 ± 8,058 intensity/cell and the bottom layer 21,415 ± 7,538 intensity/cell. A trend was observed consistently across all individual replicates despite no statistical significance **(Figure 7E)**.

To further validate this finding through functional characterization, we performed immunostaining for lubricin, a key lubricating glycoprotein secreted by intimal RA-FLSs. Lubricin expression was highest in the top layer, with a mean fluorescence intensity of 67,411 ± 13,753 intensity/cell. In comparison, lubricin expression was markedly reduced in the middle and bottom layers, with mean values of 6,838 ± 1,663 intensity/cell and 673 ± 358 intensity/cell, respectively. Tukey's comparison test showed that lubricin expression was significantly reduced in the middle layer compared with the top layer ($P < 0.01$) and further reduced in the bottom layer ($P < 0.001$), while no significant differences were detected between the middle and bottom layers **(Figure 7G)**.

Representative fluorescence images together with quantitative analyses of viability, CD55, CD90, and lubricin expression across the three spatial layers are presented in **(Figure 7).**

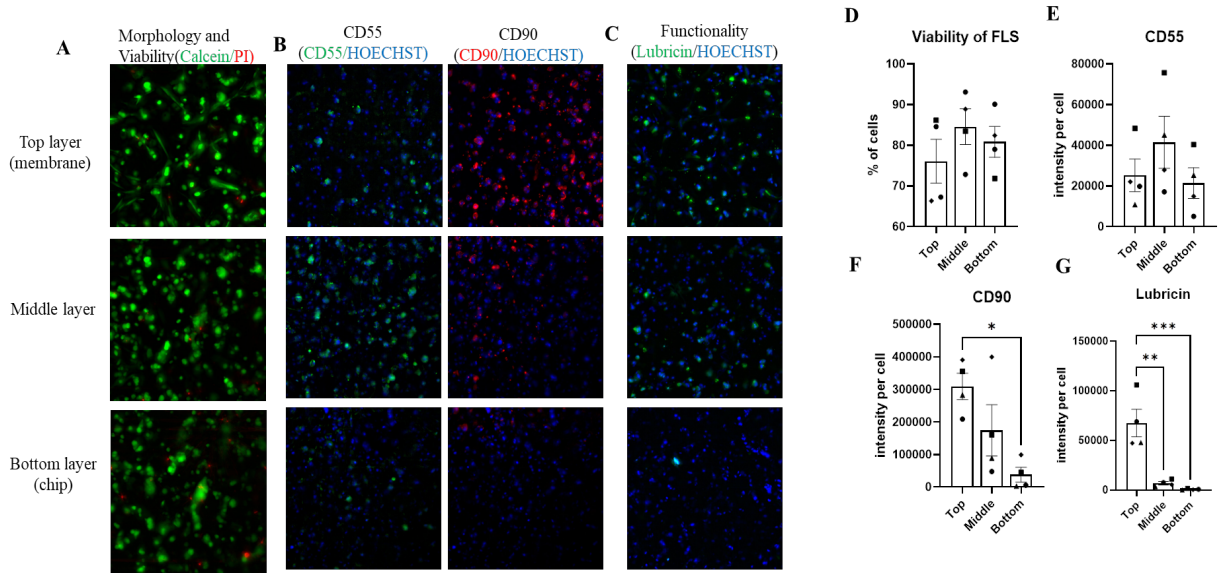

Fig. 7. The synovium-on-chip recapitulates spatial fibroblast organization and functional stratification: (A) representative MIP images showing morphology and viability of RA-FLSs (5×10^6 cells/mL in GelMA 5%) after 3 days of culture in the SoC. Images are presented as three regions obtained from Z-stack acquisition: Top, middle, and bottom layers. Cell viability was evaluated using Calcein-AM/PI staining. (B) Representative MIP images showing CD55 and CD90 across the three spatial layers. (C) Representative MIP images showing the functionality of lubricin expression across the three spatial layers. (D) Quantification of FLS viability. (E) Quantification of CD55 fluorescence intensity per cell. (F) Quantification of CD90 fluorescence intensity per cell. (G) Quantification of lubricin fluorescence intensity per cell. Data are presented as mean ± SEM, n = 4 independent biological donors. Statistical significance was determined using repeated-measures-one-way ANOVA for viability and CD55, and ordinary one-way ANOVA followed by Tukey's comparison test for CD90 and lubricin. Statistical significance is indicated as *P < 0.05, **P < 0.01, ***P < 0.001.

4.4. Spatial organization and functional stratification of RA-FLSs under inflammatory conditions

To mimic the RA inflammatory microenvironment on a chip, a cocktail of cytokines was added to the culture medium after 24-hour encapsulation, including IL-1β (10 ng/ml), IL-6 (10 ng/ml), and TNF-α (20 ng/ml). After three days of culture, cell viability, morphology, fibroblast marker expression, and lubricin production were evaluated throughout the microtissue. Fluorescence images indicated that, even after inflammatory stimulation, viable RA-FLSs were still spread across the full thickness of the hydrogel **(Figure 8A)**. In line with this, Calcein-AM/PI staining showed that cells were largely alive in the top, middle, and bottom layers of the microtissue. Quantitative analysis confirmed that cell viability remained comparable among the three layers (Top layer: 73.09 ± 8.04 %, Middle: 85.16 ± 4.13 %, and Bottom: 85.32 ± 1.66%) **(Figure 8D)**.

Even so, clear shifts in morphology were apparent: elongated, spindle-like cells were most common close to the PDMS membrane, while cells became progressively rounder and more tightly clustered toward the bottom layer.

Next, we assessed fibroblast phenotypic marker expression under inflammatory conditions. CD55 immunofluorescence appeared across all three layers **(Figure 8B)**, and quantification indicated that fluorescence intensity did not differ significantly among the top, middle, and bottom regions **(Figure 8E)**. By comparison, CD90 showed a clear spatial pattern across the SoC. Cells in the top layer showed the highest intensity with 224,906 ± 49,360. While the middle layer measured 86,547 ± 20,768, and the bottom layer dropped to 23,922 ± 16,607. Using a Kruskal-Wallis test, the analysis showed that the three layers differed overall ($P < 0.05$). Dunn's post hoc testing then identified the top layer as having significantly higher CD90 expression than the bottom layer ($P < 0.05$), whereas the remaining pairwise comparisons were not statistically significant **(Figure 8F)**.

To further investigate fibroblast functional activity under inflammatory conditions **(Figure 8C)**, the lubricin staining appeared most intense at the superficial top layer and then steadily decreased toward the middle and bottom layers of the microtissue. Quantification of lubricin fluorescence demonstrated a marked spatial distribution across the SoC. Mean fluorescence intensities were 32,028 ± 9,203 intensity per cell in the top layer, 4,491 ± 2,115 intensity per cell in the middle layer, and 361.1 ± 174.1 intensity per cell in the bottom layer. One-way ANOVA revealed a significant overall difference among the three regions ($P < 0.01$). Tukey's multiple-comparisons test showed that lubricin expression was significantly higher in the top layer compared with both the middle layer ($P < 0.05$) and the bottom layer ($P < 0.01$), whereas no significant difference was observed between the middle and bottom layers **(Figure 8G)**. Overall, the data indicate that lubricin is expressed mainly in the top layer of the SoC, then reducing toward the middle layer and bottom layer. In conclusion, these data suggest a trend of high lubricin expression in the top layer of the SoC, decreasing towards the middle and bottom layers. There was no significant difference between the middle and bottom layers, implying equal low lubricin expression in the middle and bottom layers. Representative fluorescence images together with quantitative analyses of cell viability, CD55, CD90, and lubricin expression across the three spatial layers under inflammatory conditions are presented in **(Figure 8).**

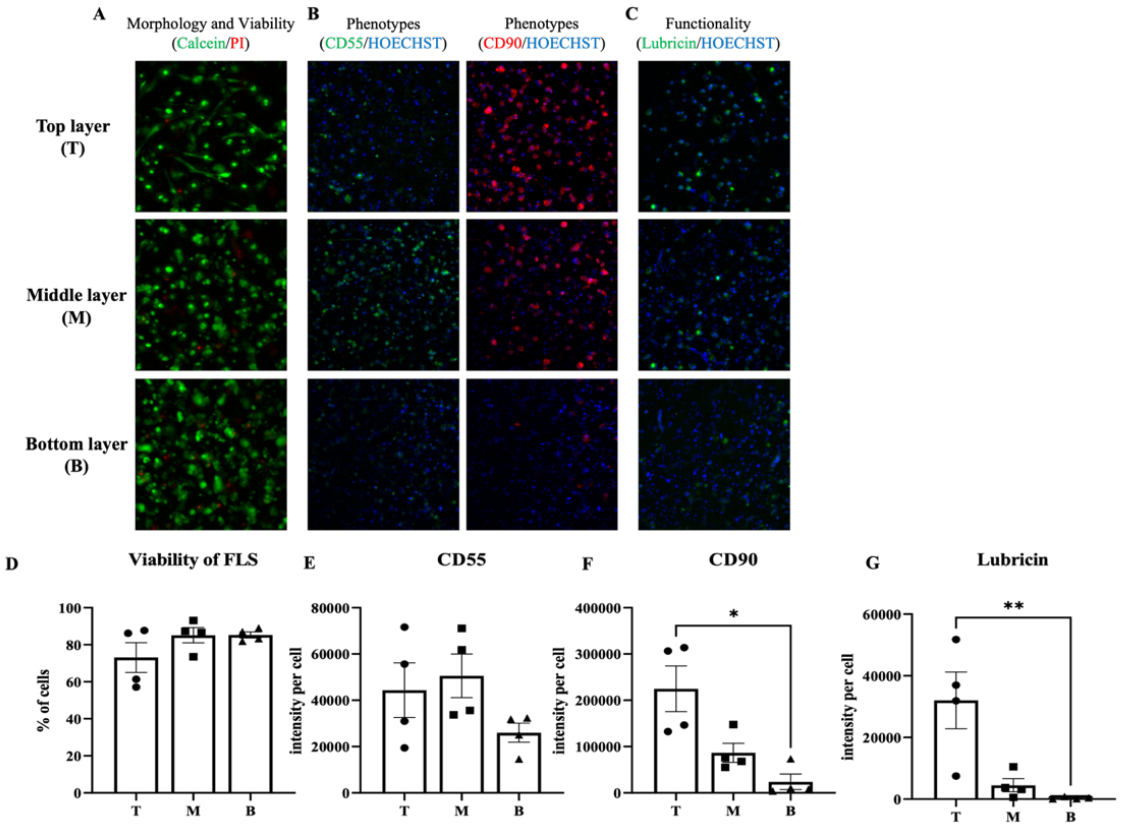

Fig. 8. Spatial layout and functional layering of RA-FLSs in the Synovium-on-a-Chip during inflammation. (A) Representative fluorescence image of FLS cultured in the top (T), middle (M), and bottom. (B) Regions of the microfluidic device. Live cells were stained with Calcein- AM (green) and dead cells with Propidium Iodide (PI, red) to assess cell viability. CD55, CD90. (C) lubricin immunofluorescence is shown in green or red, with nuclei counterstained using Hoechst (blue). (D) Cell viability was quantified across the three layers. (E) Quantification of CD55 fluorescence intensity. (F) CD90 fluorescence intensity was measured per cell. (G) Quantification of lubricin fluorescence intensity per cell. Data are presented as mean ± SEM from four independent biological samples (n = 4). Statistical significance is indicated as *P < 0.05, **P < 0.01.

4.5. Dynamic response of the SoC to inflammatory stimulation

To evaluate the influence of inflammatory stimulation on the SoC, RA-FLSs cultured under control (CTR) conditions were compared with cultures exposed to inflammatory cytokines (Inflamed). Cell morphology, viability, and the expression of CD55, CD90, and lubricin were assessed by fluorescence microscopy and quantitative image analysis **(Figure 9).** Representative fluorescence images indicated that RA-FLSs maintained their morphology in both the CTR and Inflamed conditions **(Figure 9A).** Live/dead staining showed that cells were largely viable across the two conditions. Quantitative analysis confirmed that overall cell viability remained comparable

between CTR and inflamed cultures, with no statistically significant difference detected **(Figure 9A).**

Expression of fibroblast phenotypic markers was evaluated. CD55 fluorescence intensity showed a slight increase following inflammatory stimulation (30,883 ± 9,605 intensity per cell) compared with CTR cultures (15,088 ± 3,173 intensity per cell). Although CD55 expression appeared to increase following inflammatory stimulation, this difference was not statistically significant **(Figure 9B)**. Likewise, CD90 fluorescence intensity appears to moderately reduce inflamed cultures compared with CTR groups. Quantitative analysis of CD90 fluorescence intensity showed a modest reduction following inflammatory stimulation, decreasing from 204,791 ± 64,869 intensity per cell under CTR conditions to 150,394 ± 37,442 intensity per cell in inflamed cultures. However, this difference did not reach statistical significance, indicating that inflammatory stimulation did not substantially alter CD90 expression in the overall RA-FLSs population **(Figure 9C).**

In contrast, lubricin expression was significantly affected by inflammatory stimulation. Quantitative analysis revealed a marked reduction in lubricin fluorescence intensity, decreasing from 39,562 in control cultures to 19,286 intensity per cell after cytokine treatment ($P<0.05$) **(Figure 9D).** These findings indicate that, although fibroblast viability and the expression of major phenotypic markers remained largely preserved, inflammatory cytokines substantially impaired the functional secretory activity of RA-FLSs.

Overall, the results indicate that the SoC responds to inflammatory stimulation primarily through functional rather than phenotypic changes. While cell viability and fibroblast identity remained largely stable, lubricin production was significantly reduced, indicating the establishment of an inflammation-associated functional phenotype within the microphysiological model.

Representative fluorescence images together with quantitative analyses comparing CTR and inflamed SoC cultures are presented in **(Figure 9).**

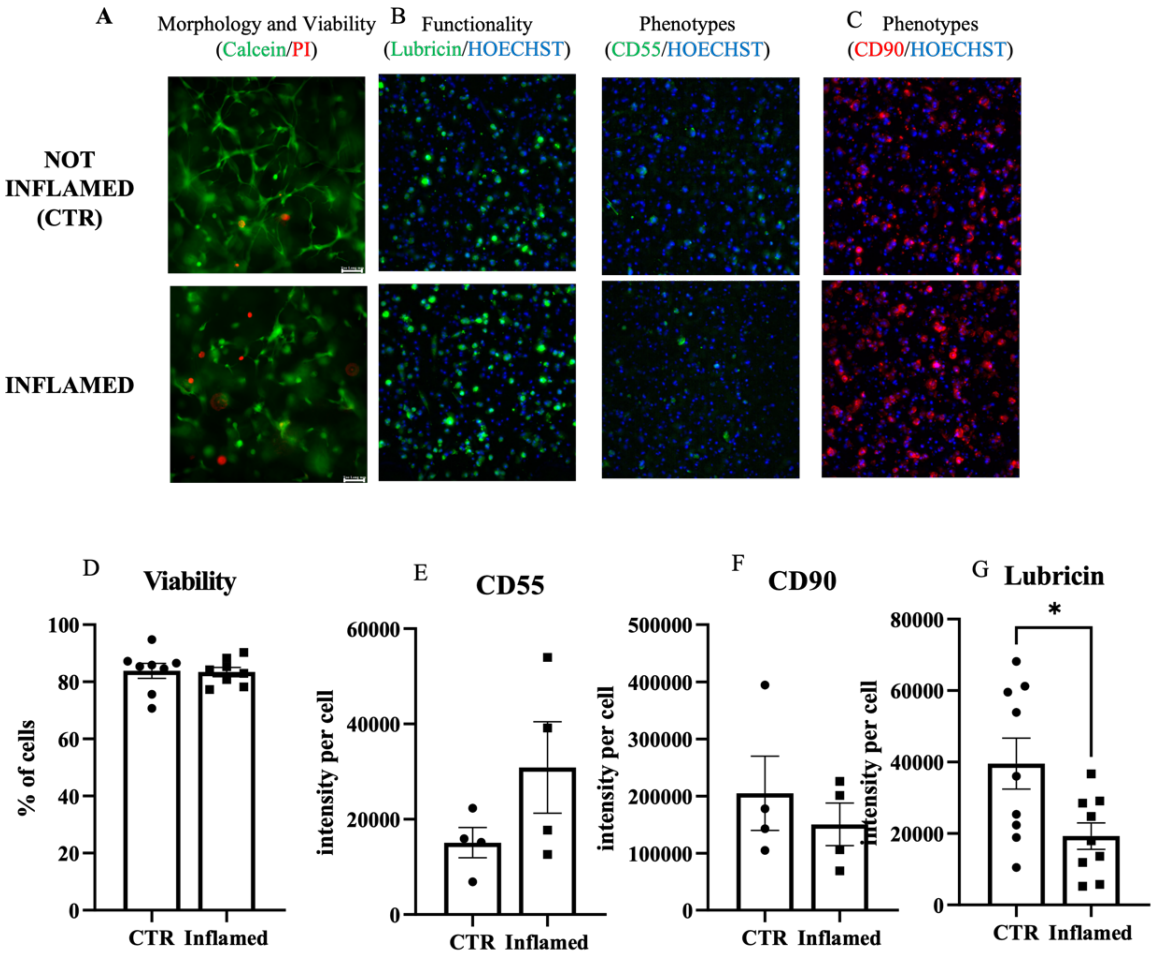

Fig. 9. The SoC dynamically responds to inflammatory stimulation. Representative fluorescence images and quantitative analyses of RA-FLSs under CTR or inflammatory (Inflamed) conditions after three days of culture. (A) Representative live/dead staining using Calcein-AM (green) and Propidium Iodide (PI) (red), showing cell viability in CTR and inflamed cultures. (B) Representative immunofluorescence images of Lubricin (green) with nuclei counterstained using Hoechst (blue). (C) Representative immunofluorescence images of CD55 (green) with Hoechst nuclear counterstaining (blue). (D) Representative immunofluorescence images of CD90 (red) with Hoechst nuclear counterstaining (blue). (E) Quantification of cell viability, expressed as the percentage of live cells, showing no significant difference between CTR and inflamed cultures (unpaired Student's t-test). (F) Quantification of fluorescence intensity per cell for CD55, CD90, and Lubricin. CD55 expression showed a slight increase and CD90 a slight decrease following inflammatory stimulation, although neither reached statistical significance (paired Student's t-test). In contrast, Lubricin fluorescence intensity per cell was significantly reduced in inflamed cultures compared with CTR (paired Student's t-test, $P < 0.05$). (G) Summary of the statistical comparison between CTR and inflamed conditions for the analyzed markers. Data are presented as mean ± SEM, and statistical significance was considered at $P < 0.05$.

5. Discussion

RA is a chronic immune-mediated disease in which persistent synovial inflammation promotes progressive cartilage and bone damage. FLS, which normally maintain the synovial extracellular matrix and produce joint lubricants such as lubricin, acquire an activated and aggressive phenotype in RA. These cells contribute directly to synovial hyperplasia, inflammatory mediator production, matrix degradation, and the persistence of joint inflammation. Therefore, understanding how RA-FLSs maintain their phenotype and function within a physiologically relevant synovial microenvironment is essential for improving disease models and identifying new therapeutic strategies (Nygaard and Firestein, 2020). Recent advances in SoC technology have enabled more physiologically relevant in vitro models by combining 3D culture with controlled microfluidic perfusion. These systems better reproduce the native synovial microenvironment, promoting cell viability, tissue-specific functions, and cellular interactions compared with conventional static cultures. Consistent with these observations, our SoC model maintained high RA-FLSs viability and preserved lubricin expression, supporting its suitability for modelling the synovial environment and studying RA (Zhang et al., 2024).

Recent evidence indicates that RA-FLSs are composed of functionally distinct subsets rather than a uniform cell population. $CD55^+$ fibroblasts are predominantly localized in the synovial lining layer, where they contribute to synovial fluid homeostasis through the production of lubricin, whereas $CD90^+$ fibroblasts are mainly found in the sublining region and are associated with extracellular matrix remodeling and inflammatory responses. The preservation of both CD55 and CD90 expression in our SoC model suggests that the platform maintains key fibroblast phenotypes and reflects the cellular heterogeneity of the native synovium, making it a relevant model for studying RA (Qian et al., 2024). Croft et al. demonstrated that FLS are organized into distinct anatomical subsets that perform specialized biological functions within the joint. Rather than representing a homogeneous cell population, lining and sublining FLS exhibit different transcriptional programs and contribute differently to tissue homeostasis and disease progression. The authors further showed that the anatomical localization of these fibroblast populations is closely associated with their biological functions, emphasizing that preserving fibroblast heterogeneity is essential for accurately modeling the native synovial microenvironment and investigating RA pathogenesis (Croft et al., 2019). FLS are organized into distinct anatomical

niches within the joint rather than being randomly distributed. Using transcriptomic profiling combined with immunofluorescence analysis, Mizoguchi et al. identified multiple fibroblast subsets with unique molecular signatures and regional localization, showing that cells residing in the lining, sublining, and perivascular regions perform specialized biological functions. These findings highlight that preserving both fibroblast heterogeneity and spatial organization is essential for accurately reproducing the physiological architecture of the synovial tissue and understanding disease-associated cellular behavior (Mizoguchi et al., 2018).

Based on these observations, we aimed at assessing if our SoC model could reproduce the spatial organization and functional heterogeneity of RA-FLSs observed *in vivo*. To address this question, we evaluated, using bioinformatic tools, cell viability, morphology, phenotypic marker expression (CD55 and CD90), and lubricin production across different regions of the engineered microtissue. This approach allowed us to investigate whether the microfluidic platform supports the development of region-specific cellular characteristics that resemble the organization of the native synovium.

The data showed that the SoC setup could keep RA-FLSs alive and allow them to arrange themselves throughout the engineered microtissue. After three days in culture, cells remained highly viable in the top, middle, and bottom regions, which points to the hydrogel scaffold, together with continuous microfluidic perfusion, as a supportive setting for routine cell maintenance. No meaningful differences in viability emerged between the three regions. Still, small shifts in morphology and where cells clustered were noticeable. In the upper region, cells tended to look more elongated and spindle-like; deeper in the construct, in the middle and lower layers, cell packing appeared higher, and shapes leaned more rounded. Taken together, these patterns indicate that the 3D microenvironment can steer how cells organize in space while leaving survival intact, and they align with the microfluidic platform's capacity to mirror structural aspects of native synovial tissue. Recent advances in SoC technology have demonstrated that microfluidic culture systems provide a more physiologically relevant environment than conventional static culture by combining 3D tissue organization with continuous medium perfusion. Such platforms better preserve fibroblast morphology, extracellular matrix deposition, and tissue-specific cellular functions while allowing the study of synovial biology under conditions that more closely resemble the native joint microenvironment. These characteristics make microfluidic models valuable tools

for investigating fibroblast behaviour and evaluating disease-related changes in RA (Thompson et al., 2023).

In our SoC model, the spatial distribution of fibroblast phenotypes was assessed by analysing the expression of CD55 and CD90, i.e., two specific surface markers of FLS, across the three regions of the hydrogel microtissue. CD55-positive fibroblasts appeared in every layer, and the middle region tended to show the strongest fluorescence. However, no statistically significant regional differences were identified, indicating that lining-associated fibroblasts remained evenly distributed within the 3D construct. CD90, on the other hand, did not follow that flat pattern. Fluorescence was clearly higher in the top layer than in the bottom layer, with the middle layer landing between the two. This regional variation suggests that the microfluidic 3D environment influences fibroblast organization and phenotype, promoting the establishment of spatial heterogeneity while preserving the coexistence of both major RA-FLSs populations. Previous studies have demonstrated that RA-FLSs are composed of phenotypically and functionally distinct subsets characterized by differential expression of CD55 and CD90. CD55-positive fibroblasts are predominantly associated with the synovial lining, where they contribute to the maintenance of the synovial surface and joint homeostasis, whereas CD90-positive fibroblasts are mainly localized in the sublining region and are involved in extracellular matrix remodeling, inflammatory responses, and interactions with infiltrating immune cells. The coexistence and spatial organization of these fibroblast populations are therefore considered essential features of healthy and diseased synovial tissue (Mizoguchi et al., 2018).

Lubricin is a key glycoprotein secreted by FLS that plays a fundamental role in maintaining joint homeostasis by reducing friction between opposing cartilage surfaces and protecting the articular cartilage from mechanical wear (Jay and Waller, 2014). Beyond its lubricating function, lubricin contributes to regulating synovial cell interactions and preserving the integrity of the joint microenvironment. Reduced lubricin production has been associated with inflammatory conditions such as RA, where impaired lubrication contributes to progressive joint dysfunction (Jay and Waller, 2014). In this study, the non-inflamed SoC model maintained lubricin expression, which suggests that the microfluidic environment sustained not only RA-FLSs survival, but their functional output as well. Looking across the hydrogel microtissue, spatial readouts showed lubricin was not evenly distributed; instead, it shifted from one region to another, pointing to an

effect of the immediate 3D surroundings on fibroblast behavior. Because lubricin is mainly produced by lining fibroblasts, seeing it within the engineered tissue supports the idea that the platform maintains a fibroblast state that remains functionally relevant. Together with the preserved expression of CD55 and CD90, these findings demonstrate that the SoC model is capable of maintaining both the phenotypic identity and the functional characteristics of RA-FLSs, closely resembling important features of the native synovial tissue. The preservation of lubricin expression in our healthy SoC model is consistent with the established role of lubricin in maintaining synovial homeostasis and joint lubrication. This suggests that the engineered microenvironment supports the functional behaviour of RA-FLSs beyond simple cell survival, further demonstrating the physiological relevance of the platform (Jay and Waller, 2014).

After inflammatory stimulation, the SoC mirrored the functional shifts typically seen in RA. Cell viability remained largely stable, whereas lubricin levels reduced markedly compared to the CTR condition, pointing to inflammation-driven loss of RA-FLSs function without widespread cell death. Meanwhile, CD55 and CD90 expression changed only slightly and did not show a statistically significant difference, which suggests that short-term inflammatory exposure mainly affected fibroblast activity rather than pushing a clear phenotypic change. Taken together, the results show that this engineered microenvironment can recapture early synovial inflammatory pathology, a stage in which functional decline shows up before major effects on survival or on phenotypic identity become apparent.

Despite the encouraging findings, this study has several limitations that should be considered. The experimental model was established using a limited number of RA patient-derived FLS samples, which may not fully represent the biological heterogeneity of RA. Furthermore, the SoC model included only RA-FLSs and did not incorporate other key cellular components of the synovial microenvironment, such as macrophages, endothelial cells, or infiltrating immune cells, which are known to contribute to disease progression. In addition, the relatively short culture period and the evaluation of a single therapeutic agent limit the assessment of long-term cellular responses and complex cell–cell interactions. Nevertheless, the present study demonstrates that the SoC platform successfully maintains RA-FLSs viability, preserves phenotypic heterogeneity, supports lubricin production, and exhibits a measurable functional response to inflammatory stimulation. Future

studies should integrate multiple synovial cell populations and extend the duration of culture to further improve the physiological relevance of the model.

Overall, the findings of this study demonstrate that the developed SoC represents a physiologically relevant 3D in vitro platform capable of preserving the RA-FLSs viability, phenotypic organization, functional protein expression, and functional characteristics of RA-FLSs while reproducing key pathological features of RA. This model therefore provides a promising tool for investigating RA synovial biology and disease-associated cellular responses under controlled microphysiological conditions.

ACKNOWLEDGMENT

The completion of this thesis marks one of the most meaningful milestones of my academic and personal journey. Studying abroad has been a life-changing experience that has allowed me to grow not only as a student and researcher but also as a person. Looking back on this journey, I feel deeply grateful to everyone who has supported, encouraged, and believed in me throughout these years.

First and foremost, I would like to express my sincere gratitude to the University of Eastern Piedmont (Università del Piemonte Orientale) and the Master's Degree Programme in Medical Biotechnology for providing me with the opportunity to pursue my studies in such an inspiring academic environment. I am thankful to all the professors and staff members whose dedication and expertise have significantly contributed to my education and professional development.

I would like to express my deepest gratitude to my supervisor, Prof. Giuseppe Cappellano, for his invaluable guidance, patience, encouragement, and continuous support throughout this research project. His scientific knowledge, constructive feedback, and willingness to answer every question greatly contributed to the successful completion of this thesis. I sincerely appreciate the trust he placed in me and the opportunity to work under his supervision.

My heartfelt thanks also go to Prof. Annalisa Chiocchetti**,** Head of the Immunomics Laboratory, for providing an excellent research environment and the opportunity to be part of the laboratory. I am sincerely grateful to Dr. Thuy Duong Nguyen for her constant guidance, technical assistance, and valuable advice during both the experimental work and data analysis. Her patience and encouragement greatly strengthened my research skills.

I would also like to thank all the members of the Immunomics Laboratory for creating such a friendly, collaborative, and supportive working atmosphere. Their willingness to share knowledge and assist whenever needed made my research experience both enjoyable and enriching.

A special word of gratitude goes to my classmates and friends at the University of Eastern Piedmont. Sharing this journey with people from different cultures has been one of the greatest experiences of my life. Your friendship, encouragement, and unforgettable memories will always remain close to my heart.

My deepest appreciation goes to my beloved wife, Mahreen Zeeshan, whose unconditional love, endless patience, encouragement, and unwavering belief in me have been my greatest source of strength. Throughout every challenge, she stood beside me with constant support and sacrifice, making this achievement possible. I am truly blessed to have her as my life partner.

Finally, I dedicate this thesis to my beloved parents and my family in Pakistan. Their unconditional love, countless sacrifices, prayers, and continuous encouragement have been the foundation of every achievement in my life. Although thousands of kilometers separated us, their faith in me never weakened. Every success I achieve belongs to them before it belongs to me. I hope this accomplishment makes them proud and serves as a small token of gratitude for everything they have done for me.

To everyone who has contributed to this journey in any way, whether academically, professionally, or personally, I offer my heartfelt thanks.

ZEESHAN AHMAD

REFERENCE

Aletaha, D., Smolen, J.S., 2018. Diagnosis and Management of Rheumatoid Arthritis: A Review. JAMA 320, 1360–1372. https://doi.org/10.1001/jama.2018.13103

Antoni, C.E., Kavanaugh, A., Kirkham, B., Tutuncu, Z., Burmester, G.R., Schneider, U., Furst, D.E., Molitor, J., Keystone, E., Gladman, D., Manger, B., Wassenberg, S., Weier, R., Wallace, D.J., Weisman, M.H., Kalden, J.R., Smolen, J., 2005. Sustained benefits of infliximab therapy for dermatologic and articular manifestations of psoriatic arthritis: Results from the infliximab multinational psoriatic arthritis controlled trial (IMPACT). Arthritis Rheum. 52, 1227–1236. https://doi.org/10.1002/art.20967

Arend, W.P., 2001. Physiology of cytokine pathways in rheumatoid arthritis. Arthritis Care Res. Off. J. Am. Coll. Rheumatol. 45, 101–106.

Boissier, M.-C., 2011. Cell and cytokine imbalances in rheumatoid synovitis. Joint Bone Spine 78, 230–234. https://doi.org/10.1016/j.jbspin.2010.08.017

Celikkin, N., Presutti, D., Maiullari, F., Fornetti, E., Agarwal, T., Paradiso, A., Volpi, M., Święszkowski, W., Bearzi, C., Barbetta, A., Zhang, Y.S., Gargioli, C., Rizzi, R., Costantini, M., 2021. Tackling Current Biomedical Challenges With Frontier Biofabrication and Organ-On-A-Chip Technologies. Front. Bioeng. Biotechnol. 9. https://doi.org/10.3389/fbioe.2021.732130

Croft, A.P., Campos, J., Jansen, K., Turner, J.D., Marshall, J., Attar, M., Savary, L., Wehmeyer, C., Naylor, A.J., Kemble, S., Begum, J., Dürholz, K., Perlman, H., Barone, F., McGettrick, H.M., Fearon, D.T., Wei, K., Raychaudhuri, S., Korsunsky, I., Brenner, M.B., Coles, M., Sansom, S.N., Filer, A., Buckley, C.D., 2019. Distinct fibroblast subsets drive inflammation and damage in arthritis. Nature 570, 246–251. https://doi.org/10.1038/s41586-019-1263-7

Damerau, A., Gaber, T., 2020. Modeling Rheumatoid Arthritis In Vitro: From Experimental Feasibility to Physiological Proximity. Int. J. Mol. Sci. 21, 7916. https://doi.org/10.3390/ijms21217916

Donlin, L.T., Jayatilleke, A., Giannopoulou, E.G., Kalliolias, G.D., Ivashkiv, L.B., n.d. Modulation of TNF-Induced Macrophage Polarization by Synovial Fibroblasts.

Finckh, A., Gilbert, B., Hodkinson, B., Bae, S.-C., Thomas, R., Deane, K.D., Alpizar-Rodriguez, D., Lauper, K., 2022. Global epidemiology of rheumatoid arthritis. Nat. Rev. Rheumatol. 18, 591–602. https://doi.org/10.1038/s41584-022-00827-y

Hitchon, C.A., El-Gabalawy, H.S., 2011. The Synovium in Rheumatoid Arthritis. Open Rheumatol. J. 5, 107–114. https://doi.org/10.2174/1874312901105010107

Jay, G.D., Waller, K.A., 2014. The biology of Lubricin: Near frictionless joint motion. Matrix Biol. 39, 17–24. https://doi.org/10.1016/j.matbio.2014.08.008

Lin, H., Lozito, T.P., Alexander, P.G., Gottardi, R., Tuan, R.S., 2014. Stem Cell-Based Microphysiological Osteochondral System to Model Tissue Response to Interleukin-1β. Mol. Pharm. 11, 2203–2212. https://doi.org/10.1021/mp500136b

Mestres, G., Perez, R.A., D'Elía, N.L., Barbe, L., 2019. Advantages of microfluidic systems for studying cell-biomaterial interactions—focus on bone regeneration applications. Biomed. Phys. Eng. Express 5, 032001. https://doi.org/10.1088/2057-1976/ab1033

Mizoguchi, F., Slowikowski, K., Wei, K., Marshall, J.L., Rao, D.A., Chang, S.K., Nguyen, H.N., Noss, E.H., Turner, J.D., Earp, B.E., Blazar, P.E., Wright, J., Simmons, B.P., Donlin, L.T., Kalliolias, G.D., Goodman, S.M., Bykerk, V.P., Ivashkiv, L.B., Lederer, J.A., Hacohen, N.,

Nigrovic, P.A., Filer, A., Buckley, C.D., Raychaudhuri, S., Brenner, M.B., 2018. Functionally distinct disease-associated fibroblast subsets in rheumatoid arthritis. Nat. Commun. 9, 789. https://doi.org/10.1038/s41467-018-02892-y

Mohan, K.H., Pai, S., Rao, R., Sripathi, H., Prabhu, S., 2008. Techniques of immunofluorescence and their significance. Indian J. Dermatol. Venereol. Leprol. 74, 415. https://doi.org/10.4103/0378-6323.42898

Monserrat Sanz, J., Bohórquez, C., Gómez, A.M., Movasat, A., Pérez, A., Ruíz, L., Diaz, D., Sánchez, A.I., Albarrán, F., Sanz, I., Álvarez-Mon, M., 2020. Methrotexate Treatment Inmunomodulates Abnormal Cytokine Expression by T CD4 Lymphocytes Present in DMARD-Naïve Rheumatoid Arthritis Patients. Int. J. Mol. Sci. 21, 6847. https://doi.org/10.3390/ijms21186847

Müller-Ladner, U., Ospelt, C., Gay, S., Distler, O., Pap, T., 2007. Cells of the synovium in rheumatoid arthritis. Synovial fibroblasts. Arthritis Res. Ther. 9, 223. https://doi.org/10.1186/ar2337

Myasoedova, E., Davis, J.M., Crowson, C.S., Gabriel, S.E., 2010. Epidemiology of Rheumatoid Arthritis: Rheumatoid Arthritis and Mortality. Curr. Rheumatol. Rep. 12, 379–385. https://doi.org/10.1007/s11926-010-0117-y

Nam, J.L., Villeneuve, E., Hensor, E.M.A., Wakefield, R.J., Conaghan, P.G., Green, M.J., Gough, A., Quinn, M., Reece, R., Cox, S.R., Buch, M.H., van der Heijde, D.M., Emery, P., 2014. A randomised controlled trial of etanercept and methotrexate to induce remission in early inflammatory arthritis: the EMPIRE trial. Ann. Rheum. Dis. 73, 1027–1036. https://doi.org/10.1136/annrheumdis-2013-204882

Nygaard, G., Firestein, G.S., 2020. Restoring synovial homeostasis in rheumatoid arthritis by targeting fibroblast-like synoviocytes. Nat. Rev. Rheumatol. 16, 316–333. https://doi.org/10.1038/s41584-020-0413-5

Odell, I.D., Cook, D., 2013. Immunofluorescence Techniques. J. Invest. Dermatol. 133, 1–4. https://doi.org/10.1038/jid.2012.455

Otero, M., Goldring, M.B., 2007. Cells of the synovium in rheumatoid arthritis. Chondrocytes. Arthritis Res. Ther. 9, 220. https://doi.org/10.1186/ar2292

Qian, H., Deng, C., Chen, S., Zhang, X., He, Y., Lan, J., Wang, A., Shi, G., Liu, Y., 2024. Targeting pathogenic fibroblast-like synoviocyte subsets in rheumatoid arthritis. Arthritis Res. Ther. 26, 103. https://doi.org/10.1186/s13075-024-03343-4

Radu, A.-F., Bungau, S.G., 2021. Management of Rheumatoid Arthritis: An Overview. Cells 10, 2857. https://doi.org/10.3390/cells10112857

Rosser, J., Bachmann, B., Jordan, C., Ribitsch, I., Haltmayer, E., Gueltekin, S., Junttila, S., Galik, B., Gyenesei, A., Haddadi, B., Harasek, M., Egerbacher, M., Ertl, P., Jenner, F., 2019. Microfluidic nutrient gradient–based three-dimensional chondrocyte culture-on-a-chip as an in vitro equine arthritis model. Mater. Today Bio 4, 100023. https://doi.org/10.1016/j.mtbio.2019.100023

Smith, M.D., Wechalekar, M.D., 2015. The synovium, in: Rheumatology. Elsevier Inc., pp. 27–32. https://doi.org/10.1016/B978-0-323-09138-1.00004-8

Smolen, J.S., Heijde, D. van der, Machold, K.P., Aletaha, D., Landewé, R., 2014. Proposal for a new nomenclature of disease-modifying antirheumatic drugs. Ann. Rheum. Dis. 73, 3–5. https://doi.org/10.1136/annrheumdis-2013-204317

Szmyrka, M., Szechinski, J., 2001. THU0123 Apoptosis markers in rheumatoid arthritis. Ann. Rheum. Dis. 60, A394–A395. https://doi.org/10.1136/annrheumdis-2001.1000

Thompson, C.L., Hopkins, T., Bevan, C., Screen, H.R.C., Wright, K.T., Knight, M.M., 2023. Human vascularised synovium-on-a-chip: a mechanically stimulated, microfluidic model to investigate synovial inflammation and monocyte recruitment. Biomed. Mater. 18, 065013. https://doi.org/10.1088/1748-605X/acf976

van Boheemen, L., van Schaardenburg, D., 2019. Predicting Rheumatoid Arthritis in At-risk Individuals. Clin. Ther., PREVENTION OF RHEUMATOID ARTHRITIS: Challenges and Opportunities to Change the Paradigm of Disease Management 41, 1286–1298. https://doi.org/10.1016/j.clinthera.2019.04.017

Weissmann, G., 2004. Pathogenesis of Rheumatoid Arthritis. JCR J. Clin. Rheumatol. 10, S26. https://doi.org/10.1097/01.rhu.0000130687.75646.44

Zhang, X., Su, R., Wang, H., Wu, R., Fan, Y., Bin, Z., Gao, C., Wang, C., 2024. The promise of Synovial Joint-on-a-Chip in rheumatoid arthritis. Front. Immunol. 15. https://doi.org/10.3389/fimmu.2024.1408501